# The K1.8BR spectrometer system at J-PARC

Keizo Agari[1], Shuhei Ajimura[2], George Beer[3], Hyoungchan Bhang[4], Mario Bragadireanu[5], Paul Buehler[6], Luigi Busso[7,8], Michael Cargnelli[6], Seonho Choi[4], Catalina Curceanu[9], Shun Enomoto[10], Diego Faso[7,8], Hiroyuki Fujioka[11], Yuya Fujiwara[12], Tomokazu Fukuda[13], Carlo Guaraldo[9], Tadashi Hashimoto[12], Ryugo S. Hayano[12], Toshihiko Hiraiwa[11], Erina Hirose[1], Masaharu Ieiri[1], Masami Iio[1], Mihai Iliescu[9], Kentaro Inoue[10], Yosuke Ishiguro[11], Takashi Ishikawa[12], Shigeru Ishimoto[1], Tomoichi Ishiwatari[6], Kenta Itahashi[14], Masaaki Iwai[1], Masahiko Iwasaki[15,14], Yutaka Kakiguchi[1], Yohji Katoh[1], Shingo Kawasaki[10], Paul Kienle[16], Hiroshi Kou[15], Yue Ma[14], Johann Marton[6], Yasuyuki Matsuda[17], Michifumi Minakawa[1], Yutaka Mizoi[13], Ombretta Morra[7], Ryotaro Muto[1], Tomofumi Nagae[11], Megumi Naruki[1], Hiroyuki Noumi[2], Hiroaki Ohnishi[14], Shinji Okada[14], Haruhiko Outa[14], Kristian Piscicchia[9], Marco Poli Lener[9], Antonio Romero Vidal[9], Yuta Sada[11], Atsushi Sakaguchi[10], Fuminori Sakuma[14,*], Masaharu Sato[12], Yoshinori Sato[1], Shin'ya Sawada[1], Alessandro Scordo[9], Michiko Sekimoto[1], Hexi Shi[12], Yoshihisa Shirakabe[1], Diana Sirghi[9,5], Florin Sirghi[9,5], Ken Suzuki[6], Shoji Suzuki[1], Takatoshi Suzuki[12], Yoshihiro Suzuki[1], Hitoshi Takahashi[1], Kazuhiro Tanaka[1], Nobuaki Tanaka[1], Hideyuki Tatsuno[9], Makoto Tokuda[15], Dai Tomono[14], Akihisa Toyoda[1], Kyo Tsukada[18], Oton Vazquez Doce[9,19], Hiroaki Watanabe[1], Eberhard Widmann[6], Barbara K. Wünschek[6], Yutaka Yamanoi[1], Toshimitsu Yamazaki[12,14], Heejoong Yim[20], and Johann Zmeskal[6]

[1]*High Energy Accelerator Research Organization (KEK), Tsukuba, Ibaraki 305-0801, Japan*
[2]*Research Center for Nuclear Physics (RCNP), Osaka University, Ibaraki, Osaka 567-0047, Japan*
[3]*Department of Physics and Astronomy, University of Victoria, Victoria BC V8W 3P6, Canada*
[4]*Department of Physics, Seoul National University, Seoul 151-742, Republic of Korea*
[5]*National Institute of Physics and Nuclear Engineering - IFIN HH, Romania*
[6]*Stefan-Meyer-Institut für subatomare Physik, A-1090 Vienna, Austria*
[7]*INFN Sezione di Torino, Torino, Italy*
[8]*Dipartimento di Fisica Generale, Università di Torino, Torino, Italy*
[9]*Laboratori Nazionali di Frascati dell' INFN, I-00044 Frascati, Italy*
[10]*Department of Physics, Osaka University, Toyonaka, Osaka 560-0043, Japan*
[11]*Department of Physics, Kyoto University, Kyoto 606-8502, Japan*
[12]*Department of Physics, The University of Tokyo, Bunkyo, Tokyo 113-0033, Japan*
[13]*Laboratory of Physics, Osaka Electro-Communication University, Neyagawa, Osaka 572-8530, Japan*
[14]*RIKEN Nishina Center, RIKEN, Wako, 351-0198, Japan*
[15]*Department of Physics, Tokyo Institute of Technology, Meguro, Tokyo 152-8511, Japan*
[16]*Technische Universität München, D-85748, Garching, Germany*
[17]*Graduate School of Arts and Sciences, The University of Tokyo, Meguro, Tokyo 153-8902, Japan*
[18]*Department of Physics, Tohoku University, Sendai 980-8578, Japan*
[19]*Excellence Cluster Universe, Technische Universität München, D-85748, Garching, Germany*
[20]*Korea Institute of Radiological and Medical Sciences (KIRAMS), Seoul 139-706, Republic of Korea*
*E-mail: sakuma@ribf.riken.jp

. . . . . . . . . . . . . . . . . . . . . . . . . . . . . . . . . . . . . . . . . . . . . . . . . . . . . . . . . . . . . . . . . . . . .

A new spectrometer system has been designed and constructed at the secondary beam line K1.8BR in the hadron hall of J-PARC to investigate $\bar{K}N$ interactions and $\bar{K}$-nuclear bound systems. The spectrometer consists of a high precision beam line spectrometer, a liquid $^3$He/$^4$He/D$_2$ target system, a cylindrical detector system that surrounds the target to detect the decay particles from the target region, and a neutron time-of-flight counter array located $\sim$15 m downstream of the target position. Details of the design, construction, and performance of the detector components are described.
. . . . . . . . . . . . . . . . . . . . . . . . . . . . . . . . . . . . . . . . . . . . . . . . . . . . . . . . . . . . . . . . .

## 1.  Introduction

The $\bar{K}N$ interaction is one of the keys to understanding meson–baryon interactions in low-energy quantum chromodynamics (QCD) incorporating three flavors in the nuclear system. Precise measurements of elementary $\bar{K}N$ interactions and investigations of $\bar{K}$-nuclear bound systems ($\bar{K}$ nuclei) are currently hot topics. The physics goal using the secondary beam line K1.8BR is to focus on a detailed investigation of the $\bar{K}N$ interaction and $\bar{K}$ nuclei.

Extensive measurements of the anti-kaonic hydrogen atom [1–3] and low-energy $\bar{K}N$ scattering [4] have shown that the $\bar{K}N$ interaction is strongly attractive, but this is still not fully understood. In particular, the $\Lambda(1405)$ resonance, which appears 27 MeV below the $K^-p$ threshold, has been the biggest issue in understanding the $\bar{K}N$ interactions and $\bar{K}$ nuclei structure [5–9]. As a consequence of the strongly attractive $I = 0$ $\bar{K}N$ interaction, the concept of $\Lambda(1405)$ as a "seed" for possible $\bar{K}$-nuclear quasi-bound states has been widely discussed in recent years. In addition, the simplest $\bar{K}$-nuclear cluster, $K^-pp$, is of special interest because it is the lightest $S = -1$ $\bar{K}$ nucleus, from which the evolution of dense $\bar{K}$ nuclei such as $K^-ppn$ and $K^-K^-pp$ is naturally expected. In recent years many theoretical works have supported the existence of the $K^-pp$ bound state, but the predicted binding energies and widths are widely divergent [5–7,10–16]. Experimentally, however, only a small amount of information is available [17,18], which is not sufficient to discriminate between a variety of conflicting interpretations.

Experiments using elementary $\bar{K}$-induced reactions are expected to clarify such controversial $\bar{K}N$ interactions and $\bar{K}$ nuclei. At the K1.8BR beam line at J-PARC, the following three new experiments with the $K^-$ beam have been proposed and approved.

### 1.1.   A search for deeply bound kaonic nuclear states by the in-flight $^3He(K^-, n)$ reaction (the E15 experiment)

The E15 experiment searches for the simplest $\bar{K}$ nucleus, $K^-pp$ [19], whose existence was predicted by the pioneering work of Y. Akaishi and T. Yamazaki [5–7]. The goal of the experiment is to investigate the structure and decay of $K^-pp$. If the deeply bound $K^-pp$ state is found to exist as predicted [5–7], we can extend our experimental study to heavier nuclei, such as $K^-ppn$, $K^-ppp$, etc., which are also predicted to be deeply bound and of high density. Such ultra-high-density matter is the gateway toward kaon-condensed matter, where the chiral symmetry is expected to be restored.

The experiment aims to identify the nature of the $K^-pp$ bound state by reconstructing the complete kinematics of the reaction channels to discriminate all background processes, such as multi-nucleon absorptions and final state interactions. An exclusive measurement is performed with the in-flight $^3$He($K^-$, $n$) reaction, which allows us to investigate the $K^-pp$ bound state, both in the formation via missing-mass spectroscopy and its decay via invariant-mass spectroscopy using the emitted

neutron and the expected decay, $K^- pp \to \Lambda p \to \pi^- pp$, respectively. The incident $K^-$ momentum of 1.0 GeV/$c$ is chosen to maximize the $K^- N$ reaction rate [20].

If both the binding energy and width of the $K^- pp$ bound state are assumed to be approximately 100 MeV/$c^2$, as indicated by recent experimental results [17,18], the missing-mass resolution of the $(K^-, n)$ reaction is required to be less than 10 MeV/$c^2$ ($\sigma$) to discriminate the $K^- pp$ signal from physical backgrounds such as the two nucleon absorption processes from $K^- + {}^3$He interactions. For the invariant-mass spectroscopy, a large acceptance detector surrounding the target system is essential. To separate the expected $K^- pp$ decay modes of $\Lambda + p$ and $\Sigma^0 + p$, the detector is designed to identify secondary charged particles from the target and to reconstruct the $K^- pp \to \Lambda + p$ decay with an invariant-mass resolution of less than 20 MeV/$c^2$ ($\sigma$). Additional information on the other decay channels such as $p + \Sigma + \pi$ will also be studied.

### 1.2. *Precision spectroscopy of kaonic helium-3 3d → 2p X-rays (the E17 experiment)*

The aim of the E17 experiment is to determine the shift and width of the 2p state of kaonic ${}^3$He and ${}^4$He atoms with a precision better than 1 eV [22]. In a recent theoretical calculation, the 2p level shift of kaonic ${}^3$He and ${}^4$He atoms was calculated by a coupled channel scheme with a phenomenological deep potential, which accommodates the existence of deeply bound kaonic nuclear states [23]. In contrast to the calculations with optical models, which provide a very small 2p level shift below 1 eV [24,25], the coupled-channel calculation claims the possibility of a large 2p level shift ($\sim$10 eV) for kaonic ${}^3$He and/or ${}^4$He atoms, depending on the strength of the $\bar{K}$-nucleus potential. Therefore, precision measurements of the energy shift of the 2p level of kaonic ${}^3$He and ${}^4$He are a matter of great interest and can impose the most stringent constraint on the $\bar{K}$-nucleus strong interaction parameters.

By stopping negative kaons in a liquid helium target and using high-resolution silicon drift X-ray detectors (SDDs), it is possible to measure the strong-interaction shift of 3d → 2p X-rays from kaonic ${}^3$He and ${}^4$He atoms. To carry out the measurement of the X rays with the world's highest precision, i.e., better than 1 eV, we will achieve better energy resolution and higher statistics than those of the E570 experiment at KEK [26] and the SIDDHARTA experiment at LNF [27,28]. In addition, we will apply the techniques that worked for E570: in-beam energy calibration with fluorescence X-rays and background reduction by a reaction vertex reconstruction.

### 1.3. *Spectroscopic study of hyperon resonances below the $\bar{K}N$ threshold via the $(K^-, n)$ reaction on the deuteron (the E31 experiment)*

The primary goal of the E31 experiment is exclusively to show the spectral function of the $\Lambda(1405)$ resonance produced in the $\bar{K}N \to \pi\Sigma$ channel via the in-flight $(K^-, n)$ reaction on the deuteron [29]. Despite many experimental attempts and theoretical analysis related to the $\Lambda(1405)$, the most fundamental unsettled question remains, "is the $\Lambda(1405)$ located at 1405 MeV/$c^2$ or at 1420 MeV/$c^2$?". So far, in the Review of Particle Physics by the Particle Data Group [21], the existence of $\Lambda(1405)$ was established using only M-matrix analysis by R. H. Dalitz et al. [30], in which the estimated mass of the $\Lambda(1405)$ is $1406.5 \pm 4.0$ MeV/$c^2$ with a full width of $50 \pm 2$ MeV/$c^2$ based on the $K^- p \to (\pi^- \Sigma(1670)^+ \to \pi^- \pi^+ \Lambda(1405)) \to \pi^- \pi^+ \pi^- \Sigma^+ \to \pi^- \pi^+ \pi^- \pi^+ n$ reaction data samples in the hydrogen bubble chamber at a kaon momentum of 4.2 GeV/$c$ [31]. In addition to the above, the new review of 2012 [20] adopted $M = 1405^{+1.4}_{-1.0}$ from J. Esmaili et al. [32] based on the old bubble chamber data of stopped $K^-$ in ${}^4$He [33].

Theoretically, the resonance has been interpreted as an $I = 0$ quasi-bound state, embedded in the $\Sigma - \pi$ continuum. In recent years, strongly attractive $\bar{K}N$ interactions were deduced from a coupled-channel approach based on the ansatz that the $K^-$ bound state is located at 1405 MeV/$c^2$, and were used to predict strongly bound and dense $\bar{K}$ nuclear states [5–7]. On the other hand, recent analyses based on the chiral unitary model claim that $\Lambda(1405)$ has a two-pole structure; one is the $\pi\Sigma$ state and the other is the $\bar{K}N$ state, which results in a resonance position of about 1420 MeV/$c^2$ in the $\bar{K}N \rightarrow \pi\Sigma$ channel and thus a much shallower binding scheme, predicting much more weakly bound $\bar{K}$ systems [8,9]. This controversy should be solved by the new experiments.

To clarify the nature of $\Lambda(1405)$, decomposition of $\Lambda(1405)$ states coupled to $\bar{K}N$ is essential. To this end, in E31, precise measurements of the $K^-d \rightarrow \pi\Sigma n$ reaction (where production is directly coupled to the $\bar{K}N$ interaction channel) will be used to study the nature of $\Lambda(1405)$. Missing-mass spectra in the inclusive $(K^-, n)$ reaction on the deuteron target will be measured with a resolution of less than 10 MeV/$c^2$ $(\sigma)$. A beam momentum of 1.0 GeV/$c$ will be used for the reasons outlined in the E15 section. All the $\Sigma^+\pi^-$, $\Sigma^-\pi^+$, and $\Sigma^0\pi^0$ final states must be identified. Therefore, the experimental requirements of E15 also satisfy those of E31. In addition to the E15 requirement, E31 also requires the detection and identification of a backward-going proton from the $\Lambda(1405) \rightarrow \pi^0\Sigma^0$ decay followed by $\Sigma^0 \rightarrow \gamma\Lambda \rightarrow \gamma\pi^- p$, because the $\Lambda(1405)$ recoils at a backward angle, i.e., the angular distribution of decay protons is boosted backward.

## 2. Detector overview

A dedicated spectrometer was designed and constructed at the K1.8BR beam line to satisfy all the experimental requirements described in the previous section. The spectrometer consists of a high precision beam line spectrometer, a liquid $^3$He/$^4$He/D$_2$ target system, a cylindrical detector system (CDS) that surrounds the target to detect the decay particles from the target region, and a neutron
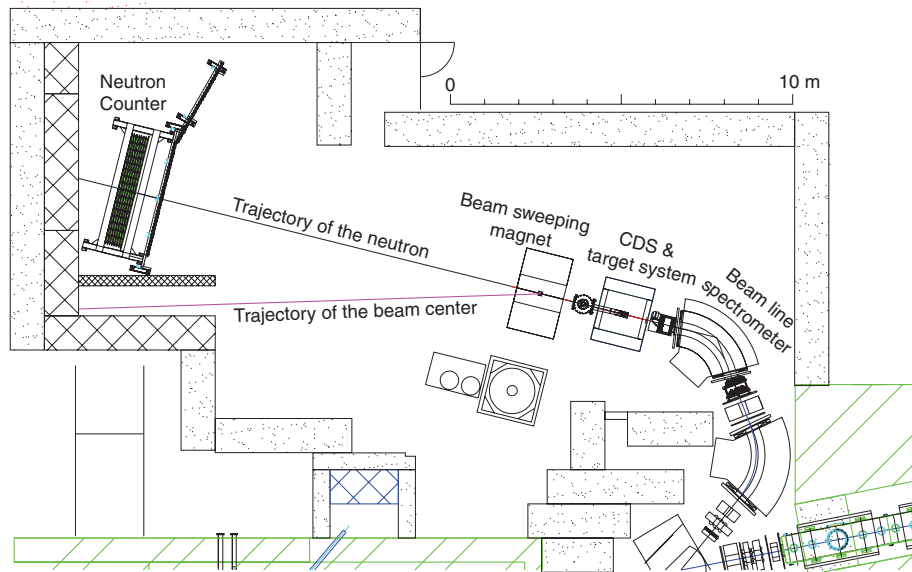


**Fig. 1.** Schematic view of the K1.8BR spectrometer. The spectrometer consists of a beam line spectrometer, a cylindrical detector system that surrounds the liquid $^3$He/$^4$He/D$_2$ target system to detect the decay particles from the target region, a beam sweeping magnet, and a neutron time-of-flight counter located $\sim$15 m downstream from the target position.

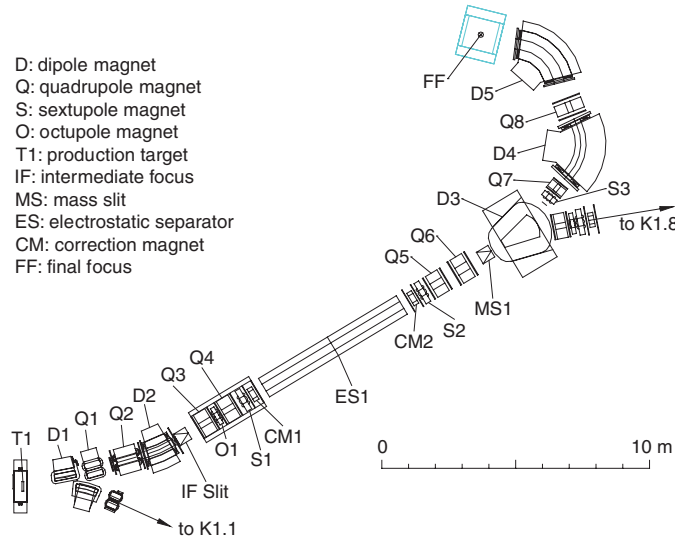**Fig. 2.** Configuration of the K1.8BR beam line in the hadron hall of J-PARC.

**Table 1.** Parameters of the K1.8BR beam line.

| | |
|---|---|
| Primary beam | 30 GeV/$c$ proton |
| Repetition cycle | 6 sec[a] |
| Flat top | 2.93 sec[a] |
| Production target | Pt(50% loss) / Ni(30% loss) |
| Production angle | 6 degrees |
| Length (T1–FF) | 31.3 m |
| Momentum range | 1.2 GeV/$c$ max. |
| Acceptance | 2.0 msr·% ($\Delta\Omega \cdot \Delta p/p$) |
| Momentum bite | ±3% |

[a]Parameters in February 2012.

time-of-flight counter array located ~15 m downstream from the target position, as shown in Fig. 1. In the following, a brief overview of the detector system at K1.8BR is provided.

The secondary beam line K1.8BR was constructed at the hadron hall of the J-PARC 50 GeV proton synchrotron (PS). The 30 GeV primary proton beam accelerated by the PS is transported to the hadron hall through the beam switching yard and is focused on the secondary-particle-production target, T1. The K1.8BR beam line branches off from K1.8 at a bending magnet downstream of an electrostatic separator, ES1, used to purify secondary beams of charged particles with momenta up to 1.2 GeV/$c$ in the K1.8BR beam line. The configuration is shown in Fig. 2 and its parameters are summarized in Table 1. The length of only 31.3 m optimizes the transport of low-momentum kaons. The intensity of a 1.0 GeV/$c$ $K^-$ beam is expected to be $8 \times 10^4$ per second based on an estimation using the Sanford–Wang formula [35–37]. An operational beam power of 270 kW (30 GeV, 9 μA proton beam) striking a 54 mm thick nickel target (30% loss target) was assumed. Details of the beam line, such as the beam line elements and optical design, are described in Ref. [34].

The beam line spectrometer is composed of beam line magnets, trigger counters, beam trackers, and a kaon identification counter. The beam line magnets, composed of an SQDQD system, are located downstream of a branching magnet D3. The beam trigger is a coincidence signal from two trigger counters located downstream from magnets D3 and D5, separated by a 7.7 m flight path. Kaon beams ranging in momentum from 0.9 to 1.2 GeV/$c$ are identified with the kaon identification counter. Pions in the beams are discriminated from kaons using the kaon identification counter, and protons are

removed by ES1. The trajectory of the kaon beam is tracked with the two beam line chambers installed across the D5 magnet. The kaon momentum is analyzed using this tracking information together with beam optics of the D5 beam line magnet to attain an expected momentum resolution of ∼0.1%. The beam line spectrometer was completed in January 2009, when the first beam was delivered to the J-PARC hadron hall.

The liquid $^3$He/$^4$He target system, whose design is based on the techniques developed for the $^4$He target used by KEK-PS E471, E549, and E570, is located at the final focus. In E17, the stopped-$K^-$ experiment, X-ray measurements are performed using the SDDs installed in the target chamber. For E31, a liquid $D_2$ target system similar to the $^3$He/$^4$He system has been developed. The liquid $^3$He/$^4$He target system was completed in 2008, and the SDDs were ready in 2010.

Decay particles from the target are detected by the CDS, which consists of a solenoid magnet, a cylindrical drift chamber (CDC), and a cylindrical detector hodoscope (CDH). The CDS has a solid angle coverage of 59% of $4\pi$. Detailed tracking information on charged particles is obtained from the CDC, which operates in a solenoidal magnetic field of 0.7 T. Particle identification is obtained using time-of-flight (TOF) together with the trigger counter. The basic CDS system was completed in 2008, and new detectors for the CDS upgrade have been developed.

A forward neutron generated by the in-flight $(K^-, n)$ reaction is detected by a forward neutron TOF counter array. TOF distance, optimized to be ∼15 m from the target, will enable us to achieve a total missing-mass resolution of less than 10 MeV/$c^2$ ($\sigma$) with ∼150 ps TOF resolution of the system. To perform efficient on-line particle identification of forward neutral particles by the neutron TOF counter, the incident beam that passes through the target is bent by a sweeping magnet placed just after the CDS. The neutron TOF counter and the sweeping magnet were installed in 2012.

## 3. Beam line detectors

A schematic view of the beam line spectrometer is presented in Fig. 3. It is composed of beam line magnets, trigger counters, beam trackers, and a kaon identification counter. The beam trigger is generated by a coincidence signal of a beam hodoscope detector (BHD) and a time zero counter (T0); the flight length between the BHD and T0 is 7.7 m. The kaon beam with momentum around 1.0 GeV/$c$ is identified by using an aerogel Cherenkov counter (AC) with a refractive index of 1.05.
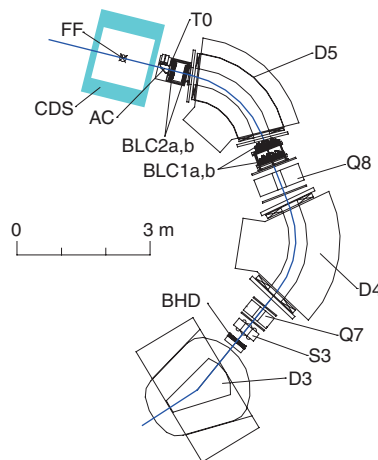


**Fig. 3.** Schematic view of the beam line spectrometer, which consists of trigger counters (BHD and T0), beam line chambers (BLC1 and BLC2), and a kaon identification counter (AC).

The kaon beam is tracked with two beam trackers—a beam line chamber 1 (BLC1) and a beam line chamber 2 (BLC2)—and the momentum of the kaon is analyzed with this tracking information together with the beam optics of the D5 beam line magnet. These basic detectors are common for all the experiments at the K1.8BR beam line.

In addition to the above detectors, an energy measurement counter (E0) and a vertex beam line drift chamber (VBDC) are used in the stopped-$K^-$ experiment E17. To stop the kaons in the target, a kaon beam of $0.9\,\mathrm{GeV}/c$ is degraded by carbon and copper blocks placed after T0. The degraded kaons are transferred into the target through E0 and the VBDC, and stopped inside the target. The reaction vertex is obtained from an incident kaon and an outgoing secondary charged particle track reconstructed by the VBDC and the CDC, respectively. By applying a correlation cut between the reaction vertex in the beam direction and the energy loss in E0, in-flight kaon decay/reaction events are rejected and continuum background events are drastically reduced as a result.

### 3.1.  Trigger counters

The BHD and T0 are segmented plastic scintillation counters located downstream of the D3 and the D5 magnet, respectively. The T0 signal is used as the event time-zero signal.

The BHD has an effective area of 400 mm (horizontal) × 160 mm (vertical) segmented into 20 units horizontally, and T0 is 160 mm (horizontal) × 160 mm (vertical) segmented into 5 units horizontally. To avoid over-concentration of the beam on one segment, T0 is rotated by 45 degrees. The BHD scintillator is made of Saint-Gobain BC412 with a unit size of 160 mm (height) × 20 mm (width) × 5 mm (thickness). The unit size of the Saint-Gobain BC420 scintillator in T0 is 160 mm (height) × 32 mm (width) × 10 mm (thickness). In both of the trigger counters, the scintillation light is transferred to a pair of 3/4 inch Hamamatsu H6612B photomultipliers that are attached to the top and bottom ends. Since the coincidence rate of the top and bottom photomultipliers will reach ∼1 M counts per spill, the high voltage bleeders of all the photomultipliers are modified to supply adequate current to the last three dynodes. Discriminated signals from the top and bottom photomultipliers are coincidenced and provide the timing of each segment. The typical TOF resolution between the BHD and T0 is 160 ps ($\sigma$) after a slewing correction is applied.

### 3.2.  Kaon identification counter

For the kaon beam trigger, the AC located downstream of T0 is used to identify the kaon. Kaons in the momentum region from $0.9\,\mathrm{GeV}/c$ to $1.2\,\mathrm{GeV}/c$, used for the experiments at K1.8BR, are clearly separated from pions.

The AC, which uses SP-50 silica aerogel produced by Matsushita Electric Works, has an effective area of 166 mm (width) × 166 mm (height) × 50 mm (thickness). Cherenkov photons radiated in the beam direction are reflected by forward optical mirrors and read out by four photomultipliers as shown in Fig. 4. The single-photon-sensitive Hamamatsu H6559UVB photomultipliers have a 3 inch diameter photocathode on UV-transparent glass windows.

AC pulse height distributions for $1.0\,\mathrm{GeV}/c$ pions and kaons, which are obtained by summing ADC spectra of the four photomultipliers, are shown in Fig. 5. In the figures, particle identifications are achieved by the TOF method between the BHD and T0 in off-line analysis. On-line pion identification is performed by the AC at a threshold level of ∼5 photoelectrons. A pion detection efficiency of 97% is achieved, whereas the misidentification ratio of a kaon as a pion is 1%.
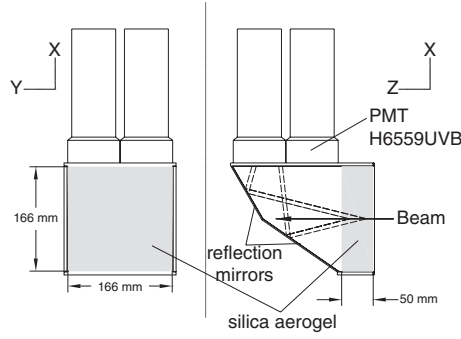
**Fig. 4.** Schematic drawings of the aerogel Cherenkov counter. Typical beam trajectories and Cherenkov light paths are shown.
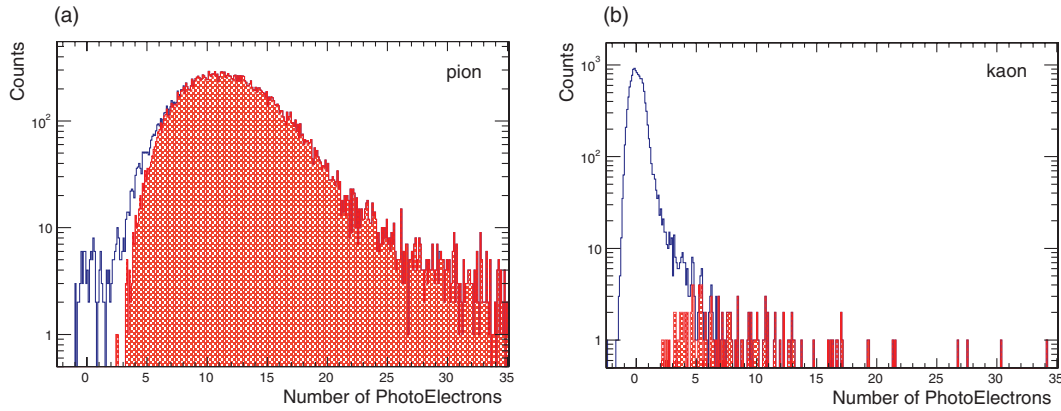


**Fig. 5.** AC pulse height distributions for $1.0\,\text{GeV}/c$ (a) pions and (b) kaons. Solid histograms represent (a) pions and (b) kaons identified with the TOF between the BHD and T0. Filled histograms represent the events identified as pions by the AC.

### 3.3. Beam line chambers

Kaon beam tracking is performed with two similar planar drift chambers, BLC1 and BLC2, installed across the D5 magnet.

BLC1 consists of two sets of the same design of drift chamber, BLC1a and BLC1b, which have 8 layers with a $UU'VV'UU'VV'$ configuration. In the $U$ and $V$ layers the wires are tilted by $\pm 45$ degrees. Each layer contains 32 sense wires with a drift length of 4 mm corresponding to an effective area of $256\,\text{mm} \times 256\,\text{mm}$. The number of readout channels is 256 for both BLC1a and BLC1b, which are installed 300 mm apart upstream of the D5 magnet.

BLC2 is similar to BLC1; BLC2 consists of two sets of the same drift chamber, BLC2a and BLC2b. Each chamber has a $UU'VV'UU'VV'$ configuration and 32 sense wires per layer, i.e, the number of readout channels is 256 for both BLC2a and BLC2b. In the $U$ and $V$ layers the wires are tilted by $\pm 45$ degrees. The drift length of 2.5 mm corresponds to an effective area of $160\,\text{mm} \times 160\,\text{mm}$. BLC2a and BLC2b are installed 275 mm apart downstream of the D5 magnet.

Both BLC1 and BLC2 use $12.5\,\mu\text{m}$ diameter gold-plated tungsten wires with 3% rhenium and $75\,\mu\text{m}$ diameter copper–beryllium wires for the sense and potential wires, respectively. The cathode planes are made of $12.5\,\mu\text{m}$ aluminized Kapton. The readout electronics of both chambers consist of a preamplifier card with amplifier-shaper-discriminator ICs (ASD, SONY-CXA3653Q [38], $\tau = 16\,\text{ns}$) mounted on the chambers, an LVDS-ECL converter, and a TDC. The output signal of

the ASD board is sent to the LVDS-ECL converter board via 7 m long twisted-pair cables. From the LVDS-ECL converter, the signal is transferred to the counting house with 50 m long twisted-pair cables. The chamber gas is an argon–isobutane mixture passed through a methylal (dimethoxy-methane) bubbler at a refrigerator temperature of 4 °C with a ratio of 76% (Ar), 20% (isobutane), and 4% (methylal). The operating voltages of BLC1 and BLC2 are set at $-1.25$ kV on both the potential wires and the cathode planes. Typical position resolutions of 150 μm and detection efficiencies of 99% for both BLC1 and BLC2 have been obtained.

### 3.4. Detectors for the stopped-$K^-$ experiment

E0, a segmented plastic scintillation counter that has an effective area of 102 mm (horizontal) × 90 mm (vertical), segmented into 3 units horizontally, is located just downstream of the degraders. The E0 scintillator is made of Eljen EJ-230 whose unit size is 102 mm (height) × 30 mm (width) × 20 mm (thickness). The scintillation light is transferred through light guides to a pair of 1 inch fine-mesh Hamamatsu H6152-01B photomultipliers attached to the top and bottom ends. The high voltage bleeders of the photomultipliers are modified to supply additional current to the last three dynodes.

The VBDC planar drift chamber is located just before the target system, hence was designed to be installable within the 30 cm inner diameter of the CDC. It is 250 mm in diameter and 73.2 mm in height and consists of 8 layers with a $UU'VV'UU'VV'$ configuration, where each layer contains 16 sense wires with a drift length of 2.5 mm corresponding to an effective area of 80 mm × 80 mm. In the $U$ and $V$ layers the wires are tilted by ±45 degrees. The sense and potential wires are the same as those for the beam line chambers. The cathode planes are made of 7.5 μm thick Kapton, both sides of which are coated with 0.1 μm aluminum with a layer of 0.0025 μm chromium as protection against oxidization. The readout electronics and gas mixture are the same as those for the beam line chambers.

For the in-flight experiments E15 and E31, E0 and VBDC are replaced by the detectors for the CDS upgrade, the TGEM-TPC, the BPC, and the BPD detectors, which are described later.

## 4. Cryogenic target systems

At the K1.8BR beam line, a liquid $^3$He/$^4$He and a liquid D$_2$ target will be used in the J-PARC E15/E17 and E31 experiments, respectively. Both target systems are combined with the CDS, which is described later. To have large acceptance for the secondary charged particles, an L-shaped cryostat was adopted to place the target cell at the center of the CDS. In this section, we present an overview of both cryogenic target systems.

### 4.1. Liquid $^3$He target system

*4.1.1. Configuration and operational procedure.* A schematic drawing of the liquid $^3$He cryostat is shown in Fig. 6 for the case of the J-PARC E15 setup. The details of the $^3$He target system can be found in a separate paper [39]. The major difference between the E15 and E17 settings is the configuration around the target cell. To maximize the acceptance for the kaonic helium X-rays in E17, eight silicon drift detectors (SDDs) will be installed around the target cell, as shown in the inset of Fig. 6. In contrast, a time projection chamber will be installed between the target vacuum chamber and the CDS in the E15 setup. Thus, the diameter of the vacuum chamber is minimized as much as possible. The major cryogenic component is divided into three sections: a $^4$He separator, a $^4$He evaporator, and a heat exchanger between $^3$He and $^4$He. The target cell is connected to the bottom of the heat exchanger with two 1 m long pipes. To reduce the radiation from room temperature
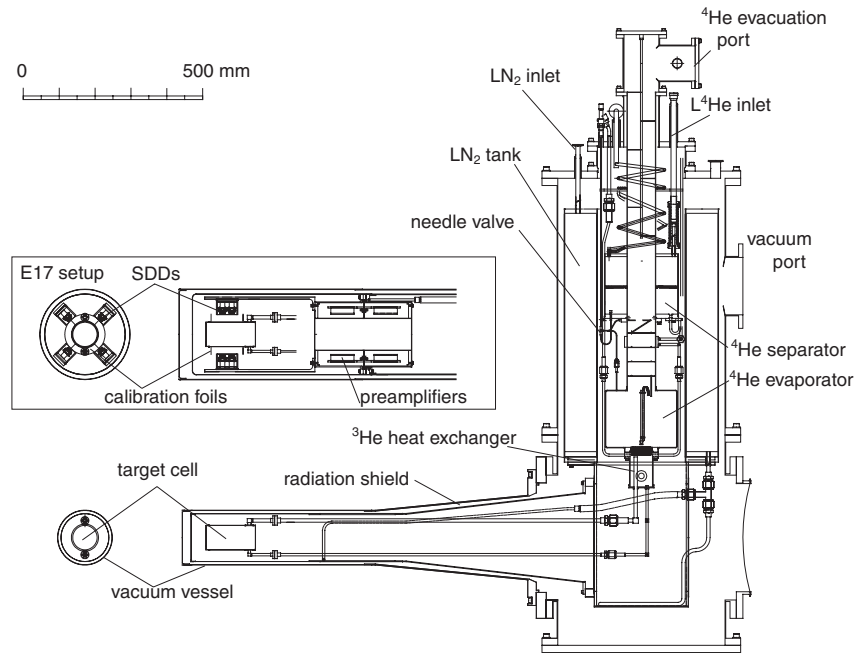
**Fig. 6.** Schematic drawing of the liquid $^3$He cryostat.

components, all low-temperature parts are covered with a radiation shield anchored to the liquid nitrogen tank (LN$_2$ tank).

The operational concept of the E15 and E17 cryostats is essentially the same. The typical start-up procedure begins with liquid nitrogen cooling. When the $^4$He separator and the LN$_2$ tank are filled, the evaporator, the heat exchanger, and the target cell are cooled by thermal conduction and radiation. After the pre-cooling, the liquid nitrogen in the separator is purged, and the liquid helium is transferred from a 1000 ℓ Dewar (not shown in the figure) to the separator by a transfer tube. The liquid flow is controlled by the pressure inside the separator evacuated by a dry pump. Liquid $^4$He inside the separator is fed to the $^4$He evaporator though a needle valve. The vapor pressure in the evaporator is reduced by a rotary pump with a pumping speed of 120 m$^3$/h, resulting in a heat-removal capability of 2.5 W at 2 K. The temperature inside the evaporator is controlled within a range of 1.3 to 2.0 K. This range is mainly determined by the flow rate from the separator to the evaporator. The lowest temperature is achieved with no flow from the separator because the liquid temperature in the separator is fairly high (4.2 K). For liquefaction of $^3$He, the heat exchanger between liquid $^4$He and gaseous $^3$He is positioned below the evaporator. The top part of the heat exchanger, where the liquid $^4$He in the evaporator is in direct contact, has a specially designed fin structure with both a width and a pitch of 0.5 mm.

A gas-tight handling system (leak rate less than $10^{-10}$ Pa·m$^3$/sec) has been constructed to store, transfer, and recover the scarce $^3$He gas. The total amount of 400 ℓ of gaseous $^3$He is stored at pressures of less than an atmosphere at room temperature in two 200 ℓ tanks. During the cooling stage, these gas tanks are connected to the heat exchanger through the gas handling system. By an effective heat contact inside the heat exchanger, gaseous $^3$He is liquefied, and the liquid $^3$He flows to the target cell (6.8 cm in diameter and 13.7 cm in length) through the lower pipe. In the last stage of cooling, most of the $^3$He gas is liquefied inside the target cell and the heat exchanger.

**Table 2.** Operational results.

| | |
|---|---|
| Vacuum level (mbar) | $<10^{-6}$ |
| Leak rate of the $^3$He system (Pa·m$^3$/sec) | $<10^{-10}$ |
| Temperature in the target cell (K) | 1.3 |
| Vapor pressure in the target (mbar) | 33 |
| Heat load to low-temperature part (W) | 0.21 |
| Liquid $^4$He consumption ($\ell$/day) | 50 |

In the L-shaped cryostat, the heat load on the target cell must be transferred effectively to the heat exchanger where the cooling power exists, otherwise boiling in the target cell occurs. To accomplish this, we applied the *siphon method* as described in Ref. [39], which uses convection of the liquid $^3$He. The liquid $^3$He warmed by the heat load inside the target cell returns to the heat exchanger through an upper pipe. In the heat exchanger, $^3$He is cooled again and fed to the target cell through the lower pipe. This makes the heat transfer between the target cell and the heat exchanger possible.

For long-term operation, it is essential to reduce the total amount of $^4$He consumed. This is because exchanging the $^4$He Dewar causes significant experimental dead time. To minimize the $^4$He consumption, we adopted *one-shot* operation. This operation consists of two modes: (I) the evaporator is filled up with liquid $^4$He supplied from the separator. (II) The $^4$He supply is stopped until the evaporator becomes empty. The operational procedure consists of a repetition of these two methods, and this reduces the total liquid $^4$He consumption due to the minimization of the transfer loss to the cryostat. The operational performance of the target system is described in the following subsection.

*4.1.2.  Operation and performance.*   Along with the operational procedure previously described, cooling tests were performed. After the $^4$He transfer, it took about 2–3 h to liquefy the $^3$He gas in the heat exchanger, achieving thermal equilibrium within 6 hours and a temperature of $1.30 \pm 0.01$ K in the target cell without flow from the separator (mode (II) in the *one-shot* operation). The liquid $^3$He density at this temperature is 0.0812 g/cm$^3$, corresponding to a thickness of 1.11 g/cm$^2$. The density fluctuation due to the temperature instability is less than 0.1%. The temperature differences between the evaporator, the heat exchanger, and the target cell are less than 0.01 K. This means that the heat transfer by the *siphon method* is working well. Furthermore, the pressure inside the heat exchanger was identical to the vapor pressure of liquid $^3$He at the corresponding temperature. Taking into consideration the remaining pressure inside the tanks, a total amount of 380 $\ell$ was condensed, giving evidence that sufficient $^3$He gas is liquefied to fill the target.

From the reduction rate of the liquid $^4$He in the evaporator, the heat load of the low-temperature region was estimated to be 0.21 W with the E15 setting. On the E17 setting, the heat load was expected to increase due to the radiation from the SDDs to the target. It was measured to be 0.39 W with the actual E17 setting, and both of these are acceptably small for long-term operation. The operational results of the cryostat with the E15 setting are tabulated below.

Finally, we note that this cryostat can be utilized as a liquid $^4$He target system by liquefying gaseous $^4$He instead of $^3$He. The operational procedure and the performance of the liquid $^4$He target are the same as those of $^3$He. The density of the liquid $^4$He is 0.145 g/cm$^3$ at 1.3 K with a stability of better than 0.1%, and the thickness is 1.99 g/cm$^2$.

*4.2.   Liquid D$_2$ target system*

For a spectroscopic study of $\Lambda(1405)$ by the $d(K^-, n)$ reaction (J-PARC E31), we have been developing a liquid D$_2$ target system. A side-view of the cryostat is shown in Fig. 7. Since we measure the
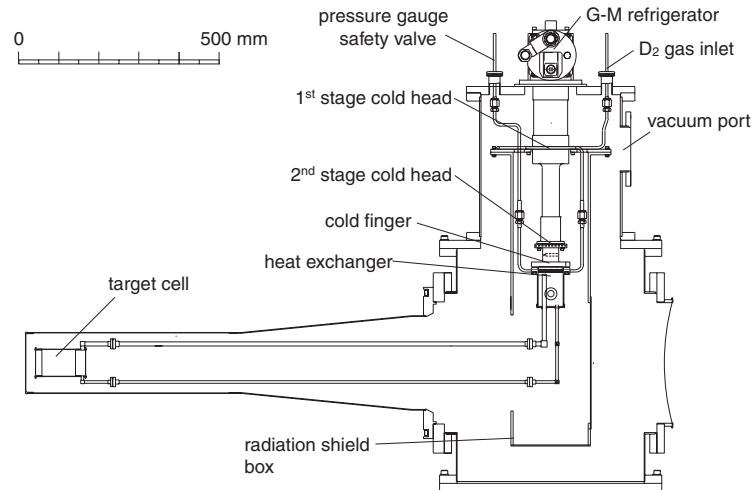
**Fig. 7.** Schematic drawing of the liquid $D_2$ cryostat.

decay products of $\Lambda(1405)$, the target cell, whose size is 6.8 cm in diameter and 12.5 cm in length, is isolated at the center of the CDS in the same way as the liquid $^3$He cryostat. The major difference from the liquid $^3$He target is that this cryostat is coolant-free. The key component of the system is a two-stage Gifford–McMahon (G–M) refrigerator (Sumitomo Heavy Industries, Ltd., RDK-145D and CSA-71A) built into the cryostat. The cooling power at the first and second stages is 35 W at 50 K and 1.5 W at 4.2 K, respectively. As it has been for the $^3$He target, a gas handling system has been constructed for the $D_2$ target. The 1000 $\ell$ of gaseous $D_2$ is stored in a tank at 2 bar at room temperature. To avoid contamination, the amount of $D_2$ gas was chosen to maintain positive pressure inside the gas system even after liquefaction in the target.

The $D_2$ gas is fed into the cryostat through the top flange. For pre-cooling, the inlet pipe for the $D_2$ gas is anchored to a copper plate attached to the first-stage cold head of the G–M refrigerator. Another inlet pipe is directly connected through the top flange to the heat exchanger. This is used to measure the $D_2$ pressure inside the heat exchanger. Since this pipe has a larger conductance, a safety valve that prevents a sudden pressure rise is also connected to it. The $D_2$ gas is cooled in the heat exchanger, where the second stage of the G–M refrigerator is thermally contacted. The structure of the heat exchanger is similar to that of the $^3$He system [39]. The main difficulty in the operation of the system is the precise control of the temperature in the heat exchanger. In the liquid $D_2$ target system, the *siphon method*, described previously, is also adopted. For effective heat transfer between the target cell and the heat exchanger, $D_2$ must be kept in a liquid state by controlling the temperature to avoid blocking of pipes by solid $D_2$. The temperature range of liquid $D_2$ is 18.7–23.8 K at 1 bar, thus the temperature should be kept around 20 K within acceptable limits. The thickness of $D_2$ along the beam is 2.13 g/cm$^2$ with a density of 0.17 g/cm$^3$ at 20 K. Since the cooling power of the second stage of the G–M refrigerator is larger than the heat load on the low-temperature parts, we have installed a heater near the cold finger to compensate the heat load. The current in the heater is controlled by a proportional-integral-derivative (PID) algorithm with an input of the temperature of the heat exchanger.

So far, we have installed the G–M refrigerator and heat exchanger in the vertical part of the cryostat. Using hydrogen gas for convenience, preliminary tests were performed to confirm the temperature stability. In these tests, the target cell was directly connected to the heat exchanger. The result showed

that the temperature of the heat exchanger is controlled within 0.2 K, which is sufficiently stable for the operation. By the end of 2012, cooling tests will be performed on the final setup with $D_2$ gas.

## 5.   Silicon drift X-ray detector

The goal of the E17 experiment is to achieve a precision measurement of both kaonic-$^3$He and -$^4$He atoms with an unprecedented accuracy of 1 eV. To achieve this precision, we employ silicon drift detectors (SDDs) with a large active area.

The concept of an SDD was originally introduced by Gatti and Rehak in 1984 [41]. The electric field parallel to the surface of the detector is generated by ring electrodes biased gradually. Electrons created by incoming X-ray absorption drift toward a collection anode placed at the center of the detector. The distinguishing feature of SDDs is the extremely small anode size, which results in the low capacitance of the detector. It is also independent of the detector active area, thus a large active area size of 100 mm$^2$ becomes possible with low capacitance. To take advantage of the low output capacitance, an FET for the first-stage amplification is directly integrated on the detector chip. It is connected to the anode with a short metal strip to minimize the stray capacitance and microphonic noise. A typical energy resolution of 150 eV is obtained at 6 keV with sufficient noise reduction. The time resolution is typically sub-micro seconds below 200 K, which is mainly determined by the drift-time distribution of electrons in silicon. In recent years, several types of SDDs with a large active area have been developed. For X-ray spectroscopy of kaonic atoms, SDDs were used in the KEK-PS E570 experiment in KEK [26] and the SIDDHARTA experiment in LNF [27].

In the J-PARC E17 experiment, 8 SDDs and reset-type preamplifiers developed by KETEK[1] were adopted. Each detector has a thickness of 0.45 mm and an active area of 100 mm$^2$. They are mounted around the liquid helium target as illustrated in the inset of Fig. 6. The acceptance for both kaonic $^3$He and $^4$He $L_\alpha$ X-rays is approximately 1% with 8 SDDs, taking into account the attenuation inside the helium target, the target cell, etc. The preamplifiers are also installed in vacuum to minimize the cable length between SDDs and preamplifiers. Output signals from the preamplifiers are connected to a CAEN N568b shaping amplifier. Semi-Gaussian outputs are provided with different shaping times of 0.5 and 3.0 μs. Output signals with 0.5 μs shaping time are used for the timing information of the SDDs in coincidence with an incoming $K^-$. Signals with 3.0 μs shaping time are recorded with two types of peak-hold ADCs, a TKO peak-hold ADC and a VME CAEN V785. For the purposes of pileup rejection, the line-shapes of the signals are also recorded by a flash ADC (SIS3301, 14 bit, 105 MHz).

To reduce the heat loads on the helium target, the SDDs must be operated at low temperature. We performed basic studies on the temperature dependence of the energy and time resolutions, and optimized the operational temperature of the SDDs to 130 K. Heat load from the preamplifiers is minimized by covering them with heat shields cooled down to 77 K. All 8 SDDs were operated successfully inside the cryostat during cooling of the liquid $^4$He target.

In November 2010, we performed commissioning of the SDDs with the secondary beam at the K1.8BR beam line. The spectrum obtained with 8 SDDs is shown in Fig. 8. Absolute energy calibration was performed with $K_\alpha$ fluorescence X-rays from titanium (4.5 keV) and nickel (7.5 keV) foils induced by the beam particles. Furthermore, we installed an iron foil at the target position to have fluorescence X-rays at an energy around 6.5 keV. As shown in the lower panel of Fig. 8, we obtained the

---

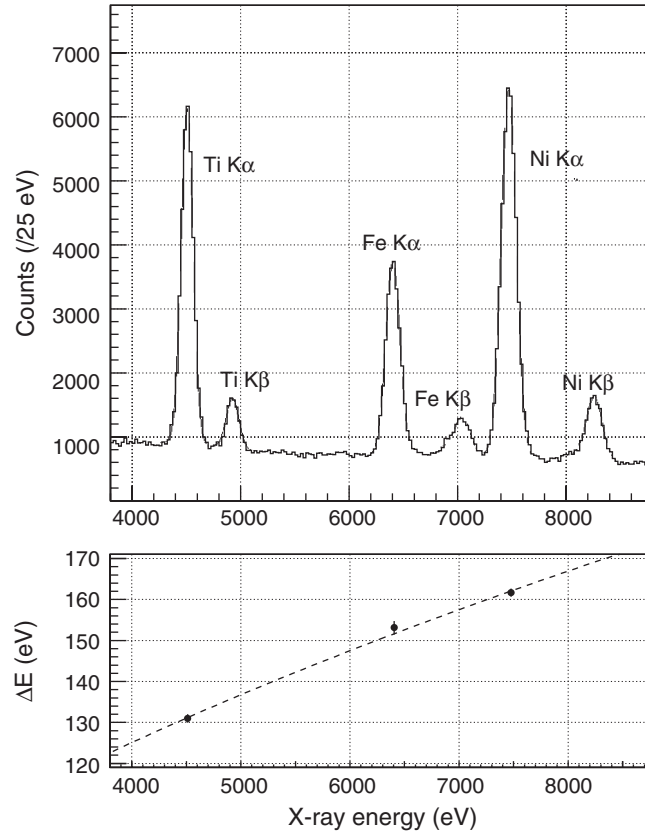[1] KETEK GmbH, Vitus-SDD without window and collimator.

**Fig. 8.** A spectrum with fluorescence x-rays induced by the beam at K1.8BR (top) and the energy dependence of the energy resolution (bottom). The dotted line represents an empirical formula described in the text.

energy resolution (FWHM) for three different energies. The dotted line in the figure is an empirical formula, $2.35\omega\sqrt{W_N^2 + FE/\omega}$, where $E$, $\omega$, $W_N$, and $F$ are incident X-ray energy, electron–hole pair creation energy, noise constant, and Fano factor, respectively. The energy dependence is well understood by the known formula. The obtained values are $F = 0.14 \pm 0.01$ and $W_N = 6.7 \pm 0.8$ with a constant of $\omega = 3.81$ eV. We achieved an energy resolution of 150 eV FWHM at an energy for kaonic $L_\alpha$ lines in $^3$He and $^4$He, which is better than the 185 eV of KEK-PS E570. This energy resolution is sufficient to achieve a precision of 1 eV with the expected statistics of kaonic $L_\alpha$ for 5000 events. The signal to noise ratio for the calibration spectrum in the commissioning is also higher than that of E570 by a factor of 3. As a result of the beam commissioning, good performance of the SDDs was achieved under realistic conditions.

## 6. Cylindrical detector system

A schematic view of the cylindrical detector system (CDS) with the target system is shown in Fig. 9. The CDS consists of a solenoid magnet, a cylindrical drift chamber (CDC), and a cylindrical detector hodoscope (CDH). The decay particles from the target are reconstructed by the CDC, which operates in a magnetic field of 0.7 T provided by the solenoid magnet. The CDH is used for particle identification and as a charged particle trigger. The CDC and the CDH are common and basic detectors for all the experiments at the K1.8BR beam line.

For in-flight experiments E15 and E31, additional detectors—a time projection chamber (TPC) with thick gas electron multipliers (TGEMs), a backward proton chamber (BPC), and a backward
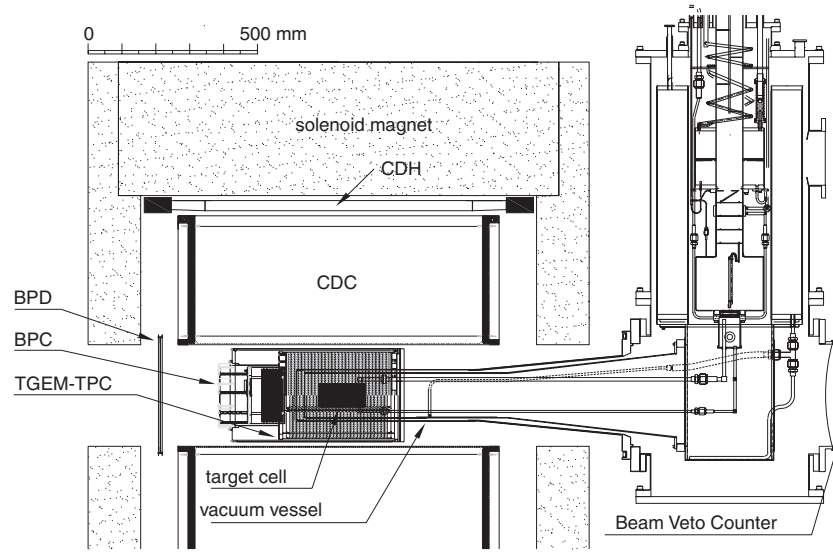
**Fig. 9.** Schematic drawing of the CDS with the target system.

proton detector (BPD)—will be installed. To realize an efficient measurement of the decay mode $K^- pp \rightarrow p\pi\Sigma$, the TPC has been developed as an inner tracker for the E15 upgrade that will be installed between the target and the CDC. The BPC and the BPD have been developed aiming to reconstruct backward-going particles that cannot be detected by the CDC. The BPC and the BPD, which are installed just upstream of the target system, enable measurement of a proton emitted from the $\Lambda(1405) \rightarrow \pi^0 \Sigma^0$ decay mode ($\Sigma^0 \rightarrow \gamma\Lambda \rightarrow \gamma\pi^- p$) by the time-of-flight method. The BPC and the BPD are also useful detectors for the E15 experiment, because the requirement of a particle in the backward direction permits an expansion of the acceptance in $\Lambda pn$ 3-body kinematical phase space.

### 6.1. Solenoid magnet

The spectrometer magnet of the CDS is of a solenoidal type, whose bore diameter is 1.18 m and whose length is 1.17 m with an overall weight of 23 tons. The design of the solenoid magnet is shown in Fig. 10. It is located on the final focus point of the K1.8BR beam line. The magnet provides a uniform field strength inside the tracking volume ($|z| < 420$ mm), whose strength is 0.7 T at the center of the magnet.

### 6.2. Cylindrical drift chamber

The CDC is a cylindrical wire drift chamber that contains 15 layers of anode wires. The structure of the CDC is shown in Fig. 11. The outer radius is 530 mm and the inner radius is 150 mm, with a total length of 950 mm. The wire length of axial layers is 838.8 mm, thus the angular coverage is $49°$ $< \theta < 131°$ in the polar angle region corresponding to a solid angle coverage of 66% of $4\pi$.

The CDC consists of two aluminum end-plates of 20 mm thickness, a 1 mm thick CFRP cylinder as the inner wall of the CDC, and six aluminum posts that are placed outside the tracking volume. The CDC uses gold-plated tungsten of 30 μm $\phi$ for the sense wires, and gold-plated aluminum of 100 μm $\phi$ for the field and guard wires. These wires are supported by feedthroughs with a bushing inserted at the end. Bushes with an 80 and 200 μm $\phi$ hole are used for the sense and field/guard wires, respectively.
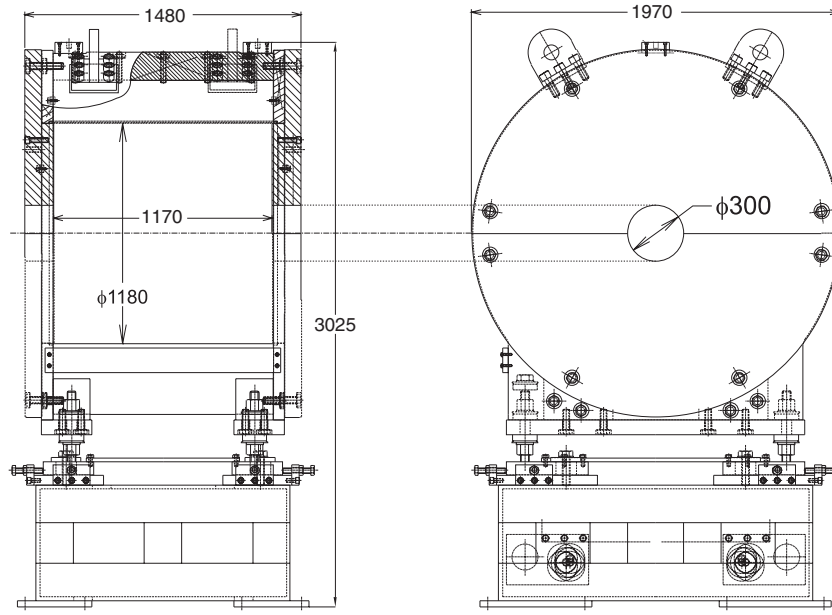
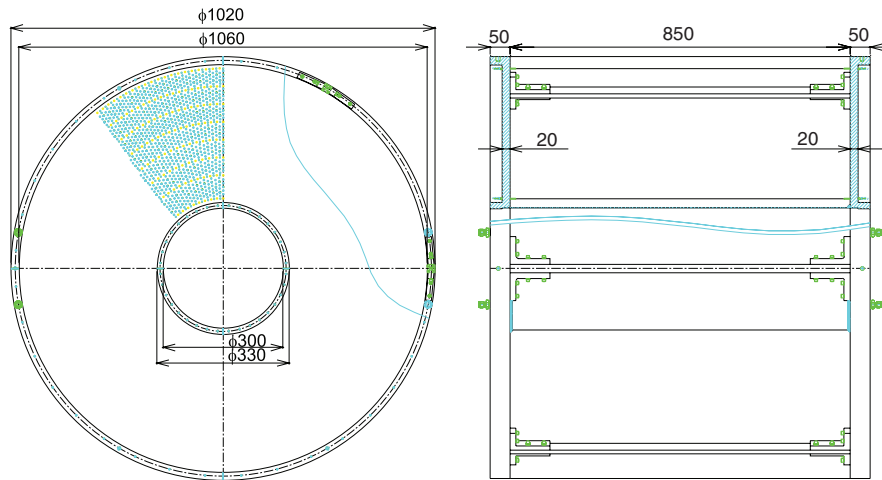**Fig. 10.** Design of the solenoid magnet (all dimensions in mm).



**Fig. 11.** Design of the CDC (all dimensions in mm). The CDC consists of two aluminum end-plates, a 1 mm thick CFRP cylinder as an inner wall, and six aluminum posts that are placed outside the tracking volume.

The CDC has 15 layers of small hexagonal cells with a typical drift length of 9 mm, which are grouped into 7 super-layers as shown in Fig. 12. Table 3 gives the detailed parameters of the wire configuration. The layers are in the radial region from 190.5 mm (layer #1) to 484.5 mm (layer #15). The 8 stereo layers tilted by about 3.5° are used to obtain longitudinal position information. The number of readout channels is 1816 and the total number of wires in the CDC is 8064.

The drift gas is 1 atm of mixed argon (50%)–ethane (50%). A high voltage is applied to the field and guard wires, and the sense wires are kept at ground potential. For the first super-layer (A1) and the second one (U1), a high voltage of $-2.8$ kV is applied to the potential wires, and $-2.7$ kV to the potential wires of the other super-layers. In addition, $-1.5$ kV, $-1.8$ kV, and $-0.6$ kV are applied to the innermost, the outermost, and the other guard wires, respectively. The readout electronics
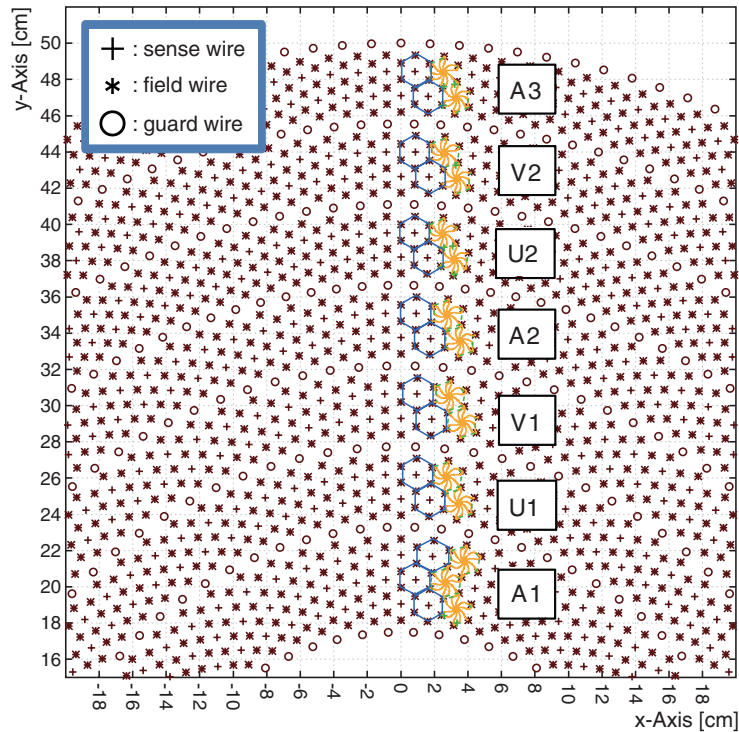
**Fig. 12.** Cell structure of the CDC.

**Table 3.** Wire configuration of the CDC.

| Super-layer | Layer | Wire direction | Radius (mm) | Cell width (degree) | Cell width (mm) | Stereo angle (degree) | Signal channels per layer |
|---|---|---|---|---|---|---|---|
| A1 | 1 | $X$ | 190.5 | 5.00 | 16.7 | 0 | 72 |
|    | 2 | $X'$ | 204.0 |      | 17.8 | 0 |    |
|    | 3 | $X$ | 217.5 |      | 19.0 | 0 |    |
| U1 | 4 | $U$ | 248.5 | 4.00 | 17.3 | −3.55 | 90 |
|    | 5 | $U'$ | 262.0 |      | 18.3 | −3.74 |    |
| V1 | 6 | $V$ | 293.0 | 3.60 | 18.4 | 3.77 | 100 |
|    | 7 | $V'$ | 306.5 |      | 19.3 | 3.94 |    |
| A2 | 8 | $X$ | 337.5 | 3.00 | 17.7 | 0 | 120 |
|    | 9 | $X'$ | 351.0 |      | 18.4 | 0 |    |
| U2 | 10 | $U$ | 382.0 | 2.40 | 16.0 | −3.28 | 150 |
|    | 11 | $U'$ | 395.5 |      | 16.6 | −3.39 |    |
| V2 | 12 | $V$ | 426.5 | 2.25 | 16.7 | 3.43 | 160 |
|    | 13 | $V'$ | 440.0 |      | 17.3 | 3.54 |    |
| A3 | 14 | $X$ | 471.0 | 2.00 | 16.4 | 0 | 180 |
|    | 15 | $X'$ | 484.5 |      | 16.9 | 0 |    |

of the CDC consists of a preamp card with ASDs (SONY-CXA3653Q, $\tau = 16$ ns), an LVDS-ECL converter, and a TDC—the same as those for the beam line chambers.

Figure 13 shows the layer efficiencies of the CDC that were obtained in the engineering run conducted in June 2012. The efficiency is evaluated by (number of tracks having hits in the relevant layer) / (number of tracks reconstructed except for hits in the relevant layer). All layers have efficiencies over 99%. In addition, the typical residual distribution of the CDC as obtained is shown in Fig. 14. A typical intrinsic resolution of 200 μm was determined in the data analysis.

The momentum resolution of the CDC, shown in Fig. 15, was estimated by a Monte Carlo simulation using the GEANT4 toolkit [42]. In the simulation, the resolution of the CDC as well as energy
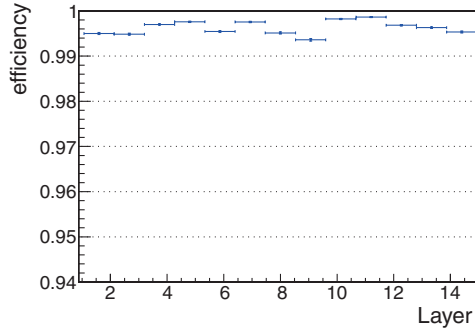
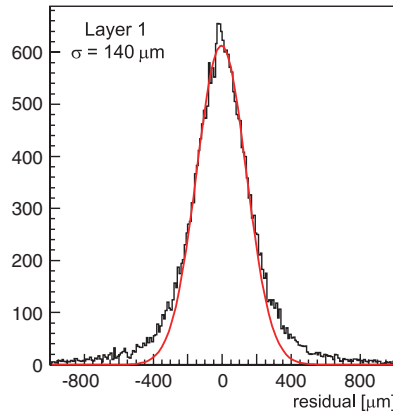**Fig. 13.** Layer efficiencies of the CDC measured in the engineering run conducted in June 2012.



**Fig. 14.** Typical residual distribution of the CDC.
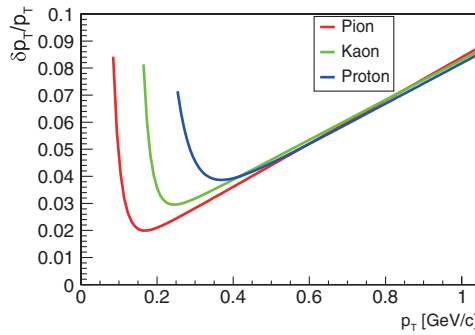


**Fig. 15.** Momentum resolution of the CDC evaluated by the Monte Carlo simulation. The $p_t$ resolutions for pions, kaons, and protons are shown.

loss and scattering in detector materials were taken into account. The calculated $p_t$ resolution was 8.4% $p_t \oplus 1.1\%/\beta$ and the estimated vertex resolution was 2.1 mm and 5.0 mm for the perpendicular and parallel directions to the beam axis, respectively.

### 6.3.  *Cylindrical detector hodoscope*

The CDH is a segmented plastic scintillation counter used for the charged particle trigger and particle identification. The CDH is located at a radius of 544 mm from the beam axis covering a polar angle range from 54 to 126 degrees corresponding to a solid angle coverage of 59% of $4\pi$.

18/28
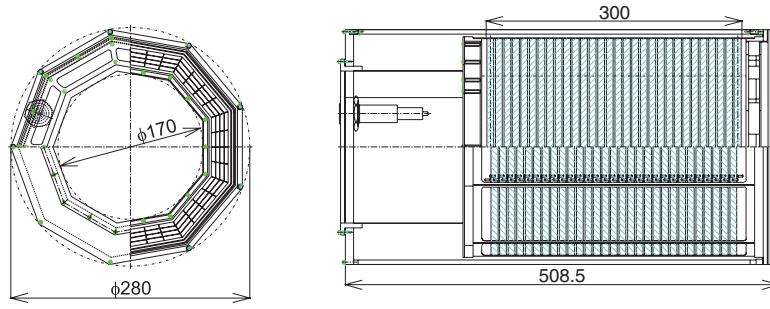
**Fig. 16.** Design of the TGEM-TPC (all dimensions in mm).

The CDH consists of 36 modules, individually mounted on the inner wall of the solenoid magnet. The scintillators are made of Eljen EJ-200, with dimensions of 790 mm in length, 99 mm in width, and 30 mm in thickness. The scintillation light is transferred through light guides to a pair of Hamamatsu R7761 fine-mesh 19-dynode photomultipliers 1.5 inches in diameter.

The CDH is operated in the 0.7 T magnetic field with a typical PMT gain of $\sim 10^6$. The measured average time resolution of the CDH without a magnetic field is $71 \pm 3$ ps $(\sigma)$, obtained with cosmic ray data.

### 6.4. TGEM time projection chamber

The TPC with TGEMs has been developed to perform precise vertex reconstruction for hyperon decays such as $\Lambda$ and $\Sigma^\pm$, as an inner tracker of the CDS. The TPC is installed between the target and the CDC. For the TPC, the spatial resolution in the $Z$ direction should be less than 1 mm, and the material budget in the CDC acceptance should be minimized.

The design of the TPC is shown in Fig. 16. It is cylindrical in shape with inner diameter 170 mm, outer 280 mm, and is filled with P-10 gas (90% Ar + 10% CH$_4$) at atmospheric pressure. The drift length is 30 cm in a field cage made from double-sided flexible printed circuits (FPC) having staggered strip electrodes with a width of 8 mm and pitch of 10 mm, connected with 1 MΩ resistors. A drift field of 150 V/cm is applied to the field cages. For amplification, a double or triple-TGEM structure is used; the TGEM is economically constructed from double-clad 400 μm thick FR4 plate using standard printed circuit board (PCB) techniques, and has mechanically drilled holes [43,44]. To reduce both the energy and the propagation probability of a discharge, the TGEM for the TPC has a nonagonal shape whose sides are subdivided into three sectors and separately connected externally to the voltage supply through high-value resistors. High voltages are applied to the double/triple-TGEM resistor chain through connectors penetrating the end cap. The gain of these nonagonal TGEMs is greater than $10^4$ with graphite electrodes having a resistance of about 30 Ω/□ both with double- and triple-TGEM configurations, as shown in Fig 17. The graphite-electrode TGEM is a new development to protect the detector and the readout electronics from damage by any occasional discharge [45]. The layout of the readout system is also nonagonal and is divided into 4 × 4 pads on each side with 4 mm long and 20 mm wide pads printed on a standard PCB (the total number of readout channels is 144). For the TPC front-end electronics, preamplifier cards with ASDs (SONY-CXA3653Q, $\tau = 80$ ns) are used, i.e., the TPC provides only beam-direction information on the tracks.

To evaluate the TPC performance, a test experiment using a positron beam of around 600 MeV/$c$ was performed at the laser-electron photon facility at SPring-8 (LEPS) [46] in November 2011. In
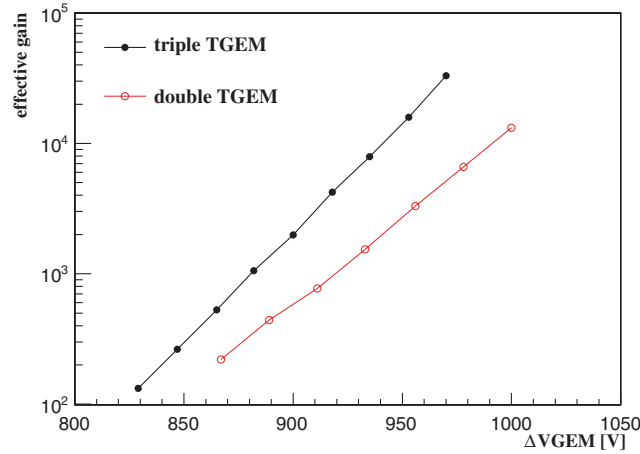
**Fig. 17.** Effective gains of the nonagonal TGEMs with the graphite electrode as a function of the voltage across each TGEM. The data for the double- and triple-TGEM configurations are shown.

the test experiment, the TPC was operated without the magnetic field with only part of the readout system installed. The typical spatial resolution obtained in the $Z$ direction was 0.95 mm and 1.9 mm at drift lengths of 30 mm and 270 mm, respectively. A tracking efficiency of over 95% was achieved independent of the drift length. The drift length dependence of the spatial resolution can be expressed as $\sigma_z^2 = \sigma_0^2 + C_d^2 \cdot z / N_{\mathrm{eff}}$, where $\sigma_z$, $\sigma_0$, $C_d$, $z$, and $N_{\mathrm{eff}}$ are total resolution, resolution without diffusion, diffusion constant, drift distance, and effective number of electrons, respectively [47,48]. With a value of $C_d = 0.34$ mm and electric field of 150 V/cm in the P-10 gas in an evaluation by the gas simulation program Magboltz [49,50], values of $\sigma_0 = 0.73$ mm and $N_{\mathrm{eff}} = 7.7$ were obtained. When operating in a magnetic field, the resolution and efficiency are expected to improve as a result of an increase in the effective number of electrons. This increase should achieve the design criteria. The TPC will be completed in 2012 followed by a performance test in which all of these basic parameters will be experimentally determined.

### 6.5. Detectors for backward protons

The BPC and BPD are installed just upstream of the target system aiming to reconstruct backward-going particles, such as pions and protons, which cannot be detected by the CDC.

The BPC is a compact circular planar drift chamber located just before the target system 168 mm in diameter and 89.7 mm in height. Figure 18 shows the design of the BPC, which consists of 8 layers with an $XX'YY'XX'YY'$ configuration, where the wires of the $Y$ layer are tilted by 90 degrees. Each layer contains 15 sense wires with a drift length of 3.6 mm corresponding to an effective area with a 111.6 mm diameter. The number of readout channels is 120. The cathode planes are made of 9 μm carbon aramid foil, and the sense and potential wires, readout electronics, and gas mixture of the BPC are the same as those for the beam line chambers. The operational voltage of the BPC is set at −1.45 kV on both the potential wires and the cathode planes. In the engineering run of 2012, individual layer efficiencies were greater than 99% and the position resolution was 150 μm.

The BPD is a plastic scintillator hodoscope array that is placed 0.5 m upstream from the final focus, inside the solenoid magnet. The size of the BPD is 350 mm (horizontal) × 340 mm (vertical) segmented into 70 units. Each scintillation counter, made of Eljen EJ-230, is 5 mm × 5 mm × 340 mm. Due to the strong magnetic field and a limited space, multi-pixel photon counters (MPPC) with

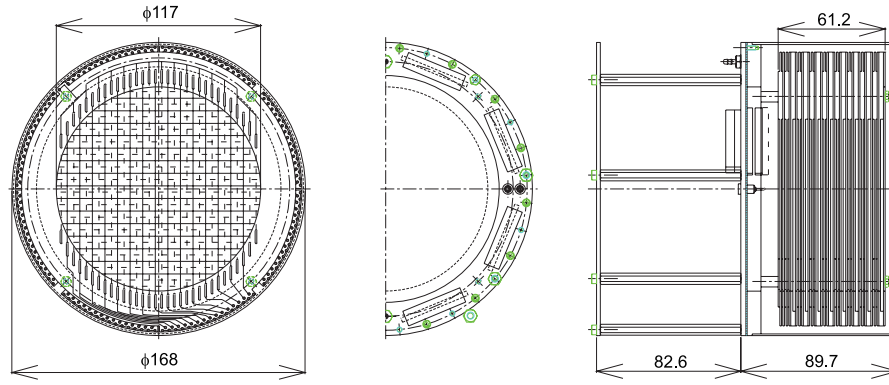**Fig. 18.** Design of the BPC (all dimensions in mm).

a 3 mm × 3 mm sensitive area were used (Hamamatsu S10362-33-050C). The MPPCs were put on both sides of each slab. Signals from the MPPCs are read out by fast timing amps (ORTEC FTA820). A typical time resolution of 160 ps was achieved in the engineering run, which is sufficient to identify a particle in the backward direction.

## 7.    Neutron time-of-flight counter and beam sweeping magnet

The neutron TOF counter, placed ~15 m away from the center of the target at 0 degrees with respect to the beam direction, detects a forward neutron generated by the in-flight $(K^-, n)$ reaction. The neutron TOF counter is an array of scintillator counters previously used by KEK-PS E549, which was reassembled for the E15 experiment. The kaon beam is swept out from the acceptance of the neutron counter by a sweeping magnet placed just after the CDS to perform efficient on-line particle identification of forward neutral particles. Charged particles within the acceptance of the neutron counter, such as those generated on the wall of the beam sweeping magnet, are vetoed by a charge veto counter located just upstream of the neutron counter. In addition, a beam veto counter is installed between the CDS and the beam sweeping magnet to reduce fake triggers caused by the decay of beam kaons after the target.

To measure both the $^3$He$(K^-, p)$ and the $(K^-, n)$ reactions, a proton TOF counter was installed. A comparison of the two kinds of missing-mass spectra will provide unique information on the isospin dependence of the kaon–nucleus ($\bar{K}$–$NN$) interaction. The proton counter is located alongside the charge veto counter, as an extended wall of the charge veto counter, on the opposite side of a beam dump to which the beam is bent by the beam sweeping magnet. Figure 19 shows a schematic view of the neutron counter, the charge veto counter, and the proton counter.

### 7.1.    Neutron time-of-flight counter

A forward neutron generated by the in-flight $(K^-, n)$ reaction is detected by the neutron TOF counter located 14.7 m away from the final focus point in which the experimental target is installed. The neutron TOF counter consists of an array of scintillation counters and has an effective volume of 3.2 m (horizontal) × 1.5 m (vertical) × 0.35 m (depth) segmented into 16-column (horizontal) × 7-layer (depth) units. The acceptance of the neutron counter is ±6.2° in the horizontal direction and ±2.9° in the vertical. Each scintillation counter has dimensions of 20 cm (width) × 150 cm (height) × 5 cm (thickness) viewed by 2 inch Hamamatsu H6410 photomultipliers attached to both long sides of the scintillator through a Lucite light guide. The scintillators for the first three layers are made of
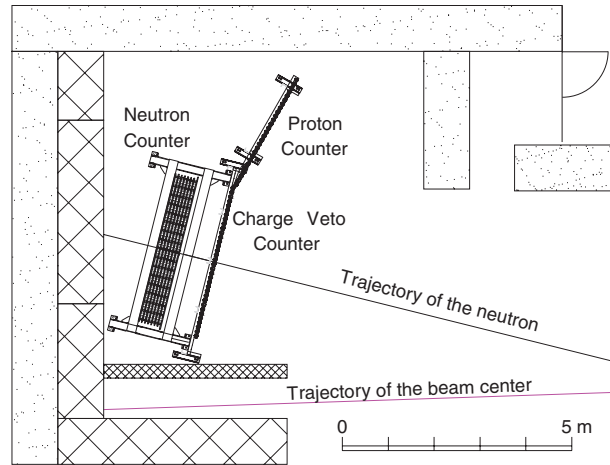
**Fig. 19.** Schematic view of the neutron counter, the charge veto counter, and the proton counter. The neutron counter is located 14.7 m away from the final focus position.

Saint-Gobain BC408, and the other four layers are made of Saint-Gobain BC412. The average time resolution of the neutron counter, measured with cosmic rays, is $92 \pm 10$ ps ($\sigma$). The detection efficiency for a $\sim$1 GeV/$c$ neutron is estimated to be $\sim$35% from the Monte Carlo simulation by the GEANT4 toolkit.

### 7.2. Beam sweeping magnet

A dipole magnet called Ushiwaka, which was used in the $\pi 2$ beam line of the 12 GeV proton synchrotron at KEK, is used as the beam sweeping magnet. It is located just downstream of the CDS. The magnet has an aperture of 82 cm (horizontal) $\times$ 40 cm (vertical) and a pole length of 70 cm, and is capable of providing a maximum field of 1.6 T. To sweep the beam away from the neutron counter acceptance window and transfer the beam to the beam dump, the magnet provides a field strength of $\sim$1.2 T at the center of the magnet.

### 7.3. Charge veto counter

The charge veto counter is located upstream of the neutron counter, 14.0 m away from the final focus point. This counter is used as a charge veto counter for the neutron detector. It has an effective area of 3.4 m (horizontal) $\times$ 1.5 m (vertical) segmented into 34 units. Each scintillation counter has dimensions of 10 cm (width) $\times$ 150 cm (height) $\times$ 3 cm (thickness), and is equipped with two 2 inch Hamamatsu H6410 photomultipliers attached to both long sides of the scintillator through a Lucite light guide. The scintillators are of Eljen EJ-200 type. The average time resolution measured with cosmic rays is $78 \pm 7$ ps ($\sigma$).

### 7.4. Proton time-of-flight counter

The proton TOF counter is installed as the extended wall of the charge veto counter. It has an effective area of 2.7 m (horizontal) $\times$ 1.5 m (vertical) segmented into 27 units. Each scintillation counter consists of a Saint-Gobain BC408 scintillator and two Hamamatsu H6410 photomultipliers attached to both long sides of the scintillator through a Lucite light guide. The average time resolution of the proton counter, obtained from cosmic ray data, is $75 \pm 6$ ps ($\sigma$).

## 7.5. *Beam veto counter*

The beam veto counter is installed between the CDS and the beam sweeping magnet. The size of the beam veto counter is 315 mm (height) $\times$ 315 mm (width) $\times$ 10 mm (thickness) made of Saint-Gobain BC408. The scintillation light transferred through a light guide is read by a 2 inch fine-mesh Hamamatsu H6154 photomultiplier. The high voltage bleeder of the photomultiplier is modified to supply additional current to the last three dynodes.

## 8. Trigger and data acquisition

### 8.1. *Trigger*

To meet experimental requirements, a dedicated hardware trigger is applied to each experiment. The kaon beam trigger is common for all experiments, whereas the main triggers for the in-flight experiments (E15 and E31) and for the stopped-$K^-$ experiment with the SDDs (E17) are substantially different. The E15 and E31 experiments use a 1.0 GeV/$c$ kaon beam, and detect a forward neutron generated by the $^3$He or $d(K^-, n)$ reaction. The E17 experiment uses a kaon beam of 0.9 GeV/$c$ that is stopped in the liquid target by using degraders located just upstream of the target system.

(1) Kaon beam trigger

The elementary beam trigger is constructed by coincidence signals from the beam line counters, the BHD and T0. The kaon beam trigger ($K_{\text{beam}}$) is selected from the beam trigger by using the kaon identification counter, i.e., a veto signal of the AC ($\overline{\text{AC}}$) defines the kaon beam. It is to be noted that (anti-)protons in the beam are eliminated upstream of the beam line by using the ES1, CM1, and CM2. A logical expression of the kaon beam trigger is given as

$$(K_{\text{beam}}) \equiv (\text{BHD}) \otimes (\text{T0}) \otimes (\overline{\text{AC}}).$$

(2) E15 main trigger

A two-level trigger logic for the in-flight $^3$He$(K^-, n)$ reaction is applied. To reconstruct the expected decay $K^- pp \to \Lambda p \to p\pi^- p$ using the CDS, an event with two or more CDH hits (CDH$_2$) is selected from the kaon beam trigger in the first level (E15$_{1\text{st}}$). In addition, no hit on the beam veto counter ($\overline{\text{BVC}}$) is required to reduce the trigger rate. In the second level (E15$_{2\text{nd}}$), an event with a forward neutron is chosen by requiring a neutron counter hit (NC) and a veto signal of the charge veto counter ($\overline{\text{TOF}}$). The E15 main trigger is given as

$$(\text{E15}_{1\text{st}}) \equiv (K_{\text{beam}}) \otimes (\text{CDH}_2) \otimes (\overline{\text{BVC}}),$$
$$(\text{E15}_{2\text{nd}}) \equiv (\text{E15}_{1\text{st}}) \otimes (\text{NC}) \otimes (\overline{\text{TOF}}).$$

(3) E17 main trigger

A two-level trigger logic is applied to measure X-rays from the kaonic helium-3 and -4 atoms. The stopped-$K^-$ trigger ($K_{\text{stopped}}$) is generated by the signal from E0 and the veto-signal from the beam veto counter with the kaon beam definition:

$$(K_{\text{stopped}}) \equiv (K_{\text{beam}}) \otimes (\text{E0}) \otimes (\overline{\text{BVC}}).$$

For the first-level trigger (E17$_{1\text{st}}$), one or more CDH hits (CDH$_1$) is required to reduce the trigger rate and obtain the reaction vertex. A hit in the SDD is required in the second level, because the timing of the SDD signal from the shaping amplifier is too late for the trigger timing of the first

level. Therefore the E17 main trigger is

$$(E17_{1st}) \equiv (K_{stopped}) \otimes (CDH_1),$$

$$(E17_{2nd}) \equiv (E17_{1st}) \otimes (SDD).$$

(4) E31 main trigger

A two-level trigger logic for the in-flight $d(K^-, n)$ reaction is applied. Since E31 measures $\Lambda(1405)$ decays into $\pi^0 \Sigma^0 \to \pi^0 \gamma \Lambda \to \pi^0 \gamma \pi^- p$ and $\pi^\pm \Sigma^\mp \to \pi^\pm \pi^\mp n$ using the CDS in addition to the forward neutron, the trigger logic is the same as that for the E15 trigger, except for a requirement for one or more CDH hits in the first level. Thus the E31 main trigger is

$$(E31_{1st}) \equiv (K_{beam}) \otimes (CDH_1) \otimes (\overline{BVC}),$$

$$(E31_{2nd}) \equiv (E31_{1st}) \otimes (NC) \otimes (\overline{TOF}).$$

### 8.2. Data acquisition system

The on-line data acquisition system (DAQ) for the experiments at K1.8BR consists of the TKO [51,52], VME, and PC Linux. The signals from the detectors are fed into ADC and TDC modules slotted into the TKO crates. In the K1.8BR experiments, 10 TKO crates are used; they are parallel read from the VME-SMP (super memory partner) [53] via a TKO SCH (super controller head). The data stored in a buffer memory of the SMP is transferred to the DAQ-PC through SBS Bit3 VME-to-PCI bridges. Additionally, the E17 experiment uses another system that consists of the VME (flash-ADC modules) and PC Linux for the readout of the SDDs. The data is written to the disk on the DAQ-PC, and transferred to a PC cluster server at RIKEN via the Internet.

## 9. Spectrometer performance

The quality of the secondary kaon beam is key for all of the experiments at K1.8BR. We have optimized the beam line since 2009 to obtain an intense and good $K/\pi$-separated kaon beam by tuning the beam line spectrometer. During a commissioning run in February 2012, beam line commissioning for $1.0\,\text{GeV}/c$ was accomplished and optimized parameters for the spectrometer were obtained. Details of the beam line performance are described in Ref. [34]. It should be noted that the typical $1.0\,\text{GeV}/c$ kaon yield normalized by an accelerator power of $1.0\,\text{kW}$ was obtained to be 10 k/spill with a $K/\pi$ ratio of 0.3, when a 60 mm thick platinum target (50% loss target) was used as the secondary-particle-production target, T1. Figure 20 demonstrates particle separation by time-of-flight between the BHD and T0. To perform on-line particle identification in the commissioning run, two Cherenkov counters located downstream of the D5 magnet were used in addition to the AC; a gas Cherenkov counter (GC, refractive index $n = 1.002$) and a water Cherenkov counter (WC, $n = 1.33$)[2]. Each particle species is clearly separated in the time-of-flight spectrum.

An engineering run with the full setup of the E15 experiment, i.e., the CDS with the liquid $^3\text{He}$ target system and the neutron counter, was also conducted in June 2012. Charged particles from the target were tracked by the CDC, and momentum information was obtained with a magnetic field of 0.7 T provided by the solenoid magnet. The event vertex was obtained from trajectories of the beam and the secondary particles that were reconstructed by the BPC and the CDC, respectively. The

---

[2] The on-line particle identification of electrons, pions, kaons, and protons is performed with coincidence signals from (GC), $(\overline{GC}) \otimes (AC)$, $(\overline{GC}) \otimes (\overline{AC}) \otimes (WC)$, and $(\overline{GC}) \otimes (\overline{AC}) \otimes (\overline{WC})$, respectively.
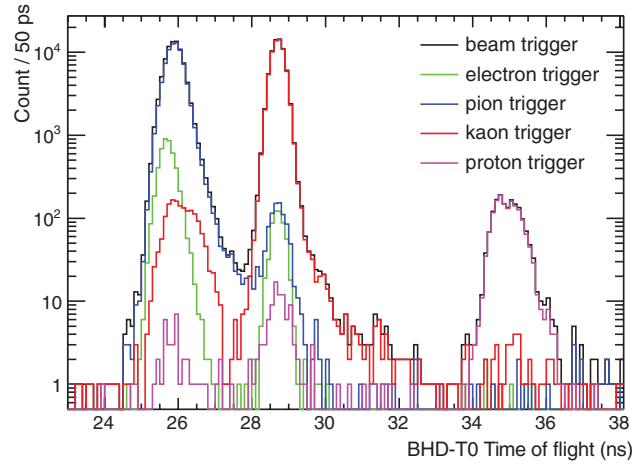
**Fig. 20.** Time-of-flight spectrum between the BHD and T0 for 1.0 GeV/$c$ positive particles with ES1 field of 50.0 kV/cm. Particle identification was performed using three Cherenkov counters.
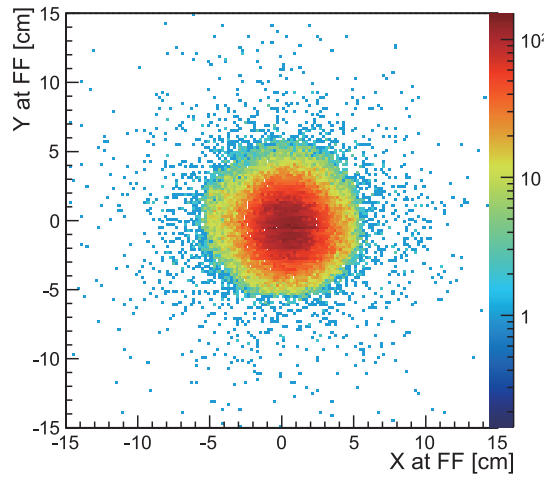


**Fig. 21.** Beam profile of the kaons at the final focus point reconstructed by the BPC.

reconstructed beam profile at the final focus point is shown in Fig. 21, and Fig. 22 demonstrates the event-vertex reconstruction in which the liquid helium target cell and transfer pipes are clearly seen.

The identification of secondary charged particles was performed by the CDH using TOF measurements together with T0. Here the flight length was calculated from the event vertex and the particle trajectory. Figure 23 shows the distributions of the momentum versus $1/\beta$. Pions, kaons, protons, and deuterons are clearly separated. The TOF resolution between T0 and the CDH is typically 160 ps ($\sigma$). Using the momentum reconstruction and the particle identification, the invariant mass of $p\pi^-$ was reconstructed as shown in Fig. 24. A clear peak of $\Lambda \to p\pi^-$ decay can be seen. As a direct demonstration of the spectrometer performance, the mass resolution of $\Lambda \to p\pi^-$ decay was compared to the expectations from the detailed detector simulation. The centroid of $\Lambda$ is obtained as $1113.6 \pm 0.1$ MeV/$c^2$ (known to be 1115.7 MeV/$c$) with a Gaussian resolution of $3.5 \pm 0.1$ MeV/$c^2$, whereas the expected centroid is $1113.4$ MeV/$c^2$ with a resolution of 3.5 MeV/$c^2$; the CDS performance has been reproduced by the simulation. The expected invariant mass resolution of the $K^- pp \to \Lambda p$ decay is evaluated to be 10 MeV/$c^2$ with the simulation, which is sufficient to satisfy the E15 requirement of less than 20 MeV/$c^2$ ($\sigma$).
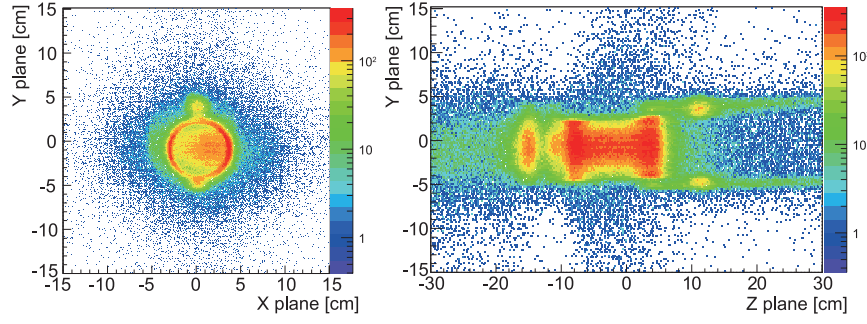
**Fig. 22.** Event vertex with the pion beam reconstructed by the CDS. The cross sections of perpendicular (left) and parallel (right) directions to the beam axis are shown. The liquid helium target cell and transfer pipes are clearly seen.
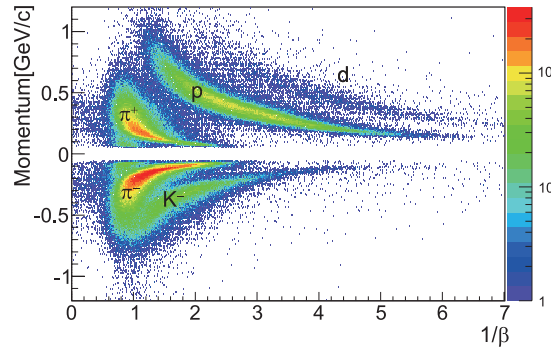


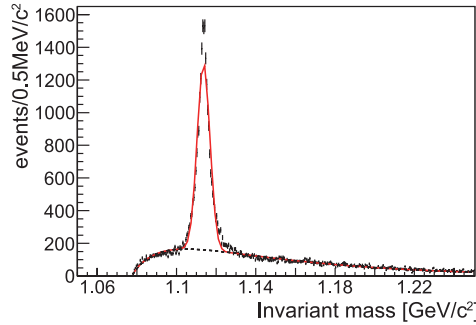**Fig. 23.** Distributions of the momentum versus $1/\beta$ obtained by the CDS.



**Fig. 24.** Invariant mass spectrum of $p\pi^-$. The spectrum is fitted with a Gaussian and a background curve. A displaced vertex cut of 2 cm is applied.

Forward-going neutral particles were also successfully detected and identified by the neutron counter in the engineering run. The resultant $1/\beta$ spectrum of the neutral particles is shown in Fig. 25, in which charged particles are vetoed by the beam veto counter and the charge veto counter. $\gamma$ rays and neutrons are clearly separated in the spectrum. The TOF resolution between T0 and the neutron counter is typically 150 ps ($\sigma$). With the measured TOF resolution, the expected missing-mass resolution for the ${}^3\text{He}(K^-, n)K^-pp$ reaction is evaluated to be 9 MeV/$c^2$ ($\sigma$), which satisfies the E15 requirement of less than 10 MeV/$c^2$ ($\sigma$).
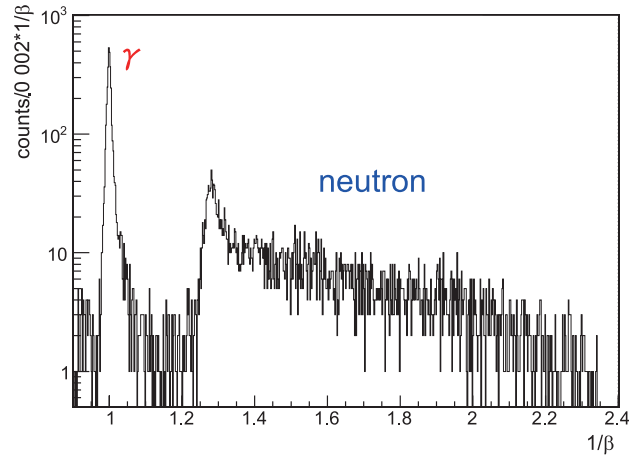
**Fig. 25.** $1/\beta$ spectrum of the neutral particles obtained by the neutron counter.

## 10.　Summary

A new spectrometer system was designed and constructed at the secondary beam line K1.8BR in the hadron hall of J-PARC. The experiments at the K1.8BR beam line aim to investigate $\bar{K}N$ interactions and $\bar{K}$-nuclear bound systems. The E15 (kaonic-nuclei search via in-flight $^3\mathrm{He}(K^-, n)$), the E17 (kaonic-atom X-ray measurement with stopped-$K^-$), and the E31 (spectroscopic study of $\Lambda(1405)$ via in-flight $d(K^-, n)$) experiments were proposed and approved at the K1.8BR beam line. The spectrometer consists of a high precision beam line spectrometer, a liquid $^3\mathrm{He}/^4\mathrm{He}/\mathrm{D}_2$ target system, a cylindrical detector system that surrounds the target to detect the decay particles from the target region, and a neutron time-of-flight counter located $\sim$15 m downstream from the target position. Commissioning of the beam line spectrometer and an engineering run with the full setup of the E15 experiment were successfully performed with a 1.0 GeV/$c$ kaon beam in February and June 2012, respectively. The results obtained show that the design goal of the spectrometer has been achieved. The experiments at K1.8BR are now ready, and the physics output will be reported in the near future.

## References

[1]　M. Iwasaki et al., Phys. Rev. Lett. **78**, 3067 (1997).
[2]　G. Beer et al., Phys. Rev. Lett. **94**, 212302 (2005).
[3]　M. Bazzi et al., Phys. Lett. B **704**, 113 (2011).
[4]　A. D. Martin, Nucl. Phys. B **179**, 33 (1981).
[5]　Y. Akaishi and T. Yamazaki, Phys. Rev. C **65**, 044005 (2002).
[6]　T. Yamazaki and Y. Akaishi, Phys. Lett. B **535**, 70 (2002).
[7]　T. Yamazaki and Y. Akaishi, Phys. Rev. C **76**, 045201 (2007).
[8]　D. Jido et al., Nucl. Phys. A **725**, 181 (2003).
[9]　T. Hyodo and A. Weise, Phys. Rev. C **77**, 035204 (2008).
[10]　N. V. Shevchenko et al., Phys. Rev. C **76**, 044004 (2007).

[11]  T. Nishikawa and Y. Kondo, Phys. Rev. C **77**, 055202 (2008).
[12]  S. Wycech and A. M. Green, Phys. Rev. C **79**, 014001 (2009).
[13]  A. Dote, T. Hyodo, and W. Weise, Phys. Rev. C **79**, 014003 (2009).
[14]  Y. Ikeda and T. Sato, Phys. Rev. C **79**, 035201 (2009).
[15]  J. Yamagata-Sekihara et al., Phys. Rev. C **80**, 045204 (2009).
[16]  T. Koike and T. Harada, Phys. Rev. C **80**, 055208 (2009).
[17]  M. Agnello et al., Phys. Rev. Lett. **94**, 212303 (2005).
[18]  T. Yamazaki et al., Phys. Rev. Lett. **104**, 132502 (2010).
[19]  M. Iwasaki and T. Nagae (E15 collaboration), 'A search for deeply-bound kaonic nuclear states by in-flight $^3$He$(K^-, n)$ reaction', J-PARC E15 proposal, (http://j-parc.jp/NuclPart/pac_0606/pdf/p15-Iwasaki.pdf).
[20]  J. Beringer et al. (Particle Data Group), Phys. Rev. D **86**, 010001 (2012).
[21]  K. Nakamura et al. (Particle Data Group), J. Phys. G: Nucl. Part. Phys. **37**, 075021 (2010).
[22]  R.S. Hayano (E17 collaboration), 'Precision spectroscopy of Kaonic Helium 3 $3d \rightarrow 2p$ X-rays', J-PARC E17 proposal, (http://j-parc.jp/NuclPart/pac_0606/pdf/p17-Hayano.pdf).
[23]  Y. Akaishi, Proc. Int. Conf. Exotic Atoms and Related Topics (EXA05), pp. 45–54 (2005).
[24]  C. J. Batty, Nucl. Phys. A **508**, 89 (1990).
[25]  S. Hirenzaki et al., Phys. Rev. C **61**, 055205 (2000).
[26]  S. Okada et al., Phys. Lett. B **653**, 387 (2007).
[27]  M. Bazzi et al., Phys. Lett. B **681**, 310 (2009).
[28]  M. Bazzi et al., Phys. Lett. B **697**, 199 (2011).
[29]  H. Noumi (E31 collaboration), 'Spectroscopic study of hyperon resonances below KbarN threshold via the $(K^-, n)$ reaction on Deuteron', J-PARC E31 proposal, (http://j-parc.jp/NuclPart/pac_0907/pdf/Noumi.pdf).
[30]  R. H. Dalitz and A. Deloff, J. Phys. G: Nucl. Part. Phys. **17**, 289 (1991).
[31]  R. J. Hemingway et al., Nucl. Phys. B **253**, 742 (1985).
[32]  J. Esmaili, Y. Akaishi, and T. Yamazaki, Phys. Lett. B **686**, 23 (2010).
[33]  B. Riley et al., Phys. Rev. D **11**, 3065 (1975).
[34]  K. Agari et al., Prog. Theor. Exp. Phys. **2012**, 02B009 (2012).
[35]  J. R. Sanford and C. L. Wang, BNL-AGS internal report 11279 (1976).
[36]  J. R. Sanford and C. L. Wang, BNL-AGS internal report 11479 (1976).
[37]  A. Yammoto, KEK Report No. 81-13 (1981).
[38]  O. Sasaki and M. Yoshida, IEEE Trans. Nucl. Sci. **46**, 1871 (1999).
[39]  M. Iio et al., Nucl. Instrum. Methods Phys. Res., Sect. A **687**, 1 (2012).
[40]  M. Sato et al., Nucl. Instrum. Methods Phys. Res., Sect. A **606**, 233 (2009).
[41]  E. Gatti and P. Rehak, Nucl. Instrum. Methods Phys. Res., Sect. A **225**, 608 (1984).
[42]  S. Agostinelli et al., Nucl. Instrum. Methods Phys. Res., Sect. A **506**, 250 (2003).
[43]  R. Chechik et al., Nucl. Instrum. Methods Phys. Res., Sect. A **535**, 303 (2004).
[44]  C. Shalem et al., Nucl. Instrum. Methods Phys. Res., Sect. A **558**, 475 (2006).
[45]  J. M. Bidault et al., Nucl. Phys. B **158**, 199 (2006).
[46]  M. Sumihama et al., Phys. Rev. C **73**, 035214 (2006).
[47]  D. R. Nygren, PEP 198 (1975).
[48]  A. R. Clark et al., *Proposal for a PEP Facility based on the Time Projection Chamber*, PEP-PROPOSAL-004 (1976).
[49]  S. F. Biagi, Nucl. Instrum. Methods Phys. Res., Sect. A **283**, 716 (1989).
[50]  S. F. Biagi, Nucl. Instrum. Methods Phys. Res., Sect. A **421**, 234 (1999).
[51]  T. K. Ohska et al., IEEE Trans. Nucl. Sci. **33**, 98 (1986).
[52]  KEK Data Acquisition Development Working Group, KEK Report 85-10 (1985).
[53]  M. Shiozawa et al., Nuclear Science Symp. and Medical Imaging Conf., pp. 632–635 (1994).